

# Synthesis, structural and biomedical characterization of hydroxyapatite/borosilicate bioactive glass nanocomposites

**Dalia Abulyazied**

University of Tabuk

**Asma Alturki**

Egyptian Petroleum Research Institute (EPRI), Nasr City

**Rasha Youness** (✉ [rhakamnrc@gmail.com](mailto:rhakamnrc@gmail.com))

University of Tabuk

**H. Abomostafa**

Menoufia University

---

## Research Article

**Keywords:** Bioactive glass, Hydroxyapatite, Nanocomposites, Structural characterization, Biomedical characterization

**Posted Date:** March 23rd, 2021

**DOI:** <https://doi.org/10.21203/rs.3.rs-334664/v1>

**License:**  This work is licensed under a Creative Commons Attribution 4.0 International License.

[Read Full License](#)

---

**Version of Record:** A version of this preprint was published at Journal of Inorganic and Organometallic Polymers and Materials on July 14th, 2021. See the published version at <https://doi.org/10.1007/s10904-021-02070-6>.

# Abstract

In this work, a borosilicate glass sample ( $5\text{SiO}_2\text{-}45\text{B}_2\text{O}_3\text{-}20\text{Na}_2\text{O}\text{-}25\text{CaO}\text{-}5\text{Ag}_2\text{O}$ ) was added to nano-sized carbonated hydroxyapatite (CHA) powders with different contents up to 20 wt.% to improve the bioactivity, antibacterial effect, physical and mechanical properties of the resulting nanocomposites. Then, these samples were mixed, milled with a high-energy ball mill, sintered at  $700^\circ\text{C}$  and subjected to X-ray diffraction (XRD) technique, Fourier transform infrared (FTIR) spectroscopy and scanning electron microscopy (SEM) to examine their structure, chemical composition and microstructure, respectively. Furthermore, the physical and mechanical properties of the sintered nanocomposites were also measured. Moreover, the in vitro bioactivity of the prepared nanocomposites was examined with XRD and SEM. Additionally, the antibacterial behavior of these samples was tested against *E. coli* and *S. aureus* by the disc-diffusion method. The results obtained pointed out that the sample with the highest content of BG possessed the best bioactivity, antibacterial effect, physical and mechanical properties.

## 1. Introduction

As a result of the enormous improvements in medicine, the life span of people around the world has been increased, forcing researchers to constantly develop new prostheses for use in bone repair purposes [1]. In this context, many biomaterials are used to achieve this goal including various metals and their alloys, bioactive glasses, glass-ceramics, calcium phosphates and calcium silicates. It is necessary to point out that the biomaterial selected should possess suitable biological characteristics bearing in mind that bioactivity is the most important biological characteristic required. Moreover, the implants must be able to induce cell proliferation in addition to facilitating the induction of bone. It is worth to note that these attractive characteristics are closely related to the surface properties of the implant [2]. In response to these facts, scientists believe that bioactive materials including some calcium phosphate (Ca-P) compounds and bioactive glasses could be greatly useful for achieving this goal [3].

Hydroxyapatite (HA;  $\text{Ca}_{10}(\text{PO}_4)_6(\text{OH})_2$ ) belongs to the family of Ca-P and is naturally present in mineralized human and animal tissues, thus, it has many amazing properties such as high surface area, fair bioactivity, excellent biocompatibility, etc. In addition, better biological properties can be obtained through the incorporation of carbonate ( $\text{CO}_3$ )<sup>2-</sup> ions in its crystal structure forming carbonated hydroxyapatite (CHA). Furthermore, the preparation of HA in the nano-scale range also aids in improving the surface properties of HA [4, 5]. Despite these wonderful characteristics, HA possesses poor mechanical properties along with a relatively slow bone bonding ability and its inability to prevent bacterial growth on its surface which lead to thinking of a solution to overcome these obstacles such as adding some elements or ceramics to enhance the abovementioned properties [6–8].

During the past decades, bioactive glasses (BGs) have gained much attention due to their ability to gradually dissolve when introduced into the human body causing a controlled release of some ions that act to encourage bone bonding capacity [1]. It is known that bioactive glass was first discovered by the efforts of Hench *et al.* [9] in the 1970s and since then, extensive efforts have been made to develop and

discover new types of BGs to be ideal candidates for the purpose of bone replacement. According to the literature [10, 11], an important benefit of these glasses is their ability to stimulate the body's own repair process called "osteostimulation". One of the major groups of these glasses is the borosilicate one which deserved the attention of a handful of researchers as a successful scaffold material due to its faster absorption rate compared to silicate glass [12].

Certainly, the most serious problems facing patients who undergo orthopaedic surgery is surgical site infection. In this regard, *S. aureus* causes about 37% of this surgical infection. Based on this information, it is best to incorporate an antibacterial agent into the biomaterial of choice to help kill this undesirable bacterial and spare the patient from potential harm [13]. For this important point, silver oxide ( $\text{Ag}_2\text{O}$ ) can be incorporated into the selected glass system to help avoid this drawback as the Ag cations exhibit an excellent antimicrobial behavior against broad spectrum of microbes [14]. Based on the attractive characteristics of HA and BGs, their combination may bring amazing properties such as suitable mechanical properties, excellent bioactivity and good osteoinductivity for use in various biomedical applications [15].

The mechanical alloying (MA) method can be used to produce desirable composites that are in the nano-scale range to obtain suitable biomaterials with good mechanical and biological properties. It is essential to note that this route depends on various milling conditions such as speed, time, size of powders, etc. [16, 17]. This work aimed to enhance the in vitro bioactivity, antibacterial behavior and mechanical properties of HA through a successive addition of BGs contents to prepare nanocomposites with excellent bioactivity, high antibacterial effect and appropriate mechanical properties.

## 2. Experimental Procedure

### 2.1 Preparation of bioactive glass (BG) samples

Glass system has been prepared by melting the starting materials ( $\text{SiO}_2$ ,  $\text{H}_2\text{BO}_3$ ,  $\text{Na}_2\text{CO}_3$ ,  $\text{CaCO}_3$  and  $\text{AgNO}_3$ ) in a platinum crucible at 1100 °C for 2 h in air. In order to ensure a homogenous mixing of all reactants and get a bubble-free sample, the molten liquid was stirred to ensure homogenous mixing of all constituents. Then, the batches were poured in a mold with the desired shape and instantly put in another muffle to be annealed at about 380–400 °C for 1 h. Subsequently, the muffle was switched off and the temperature decreased to room temperature with a rate of 25 °C/h. The nominal composition of the prepared glass system is tabulated in Table 1.

### 2.2. Preparation of CHA nanopowders

CHA nanopowders have been successfully prepared and well-characterized according to the described methods in our recent published articles [18-20]. Briefly, high-energy ball mill has been utilized using calcium carbonate ( $\text{CaCO}_3$ ) and calcium hydrogen phosphate dihydrate ( $\text{CaHPO}_4 \cdot 2\text{H}_2\text{O}$ ) as raw materials for the preparation of HA. It is worth to note that the success of mechanochemical synthesis method to

produce HA is highly dependent upon ball-to-powder ratio (BPR) and milling time as they promote the occurrence of reaction.

### **2.3. Preparation of CHA/BG nanocomposites powders**

The CHA and BG, based on their respective wt%, as represented in Table 2, were mechanically blended for 10 h using BPR equals to 1:2 and the balls diameters were 10 mm. Then, these mixtures were milled for 5 h in a planetary ball mill (type MTI SFM (QM-3SP2)) operating at 400 rpm as a rotation speed and BPR = 20:1. It is worth to mention that the milling has been performed under dry condition.

### **2.4. Measurement of the physical and mechanical properties of CHA/BG nanocomposites**

According to the recent articles of Taha *et al.* [21,22], the milled powders were pressed into pellets of 16 mm in diameter and 4 mm in length using hydraulic press at 50 MPa. Archimedes' method (ASTM: B962-13) was employed to determine the bulk density and apparent porosity of the sintered samples at 700 °C.

According to Refs. [23-25], the microhardness of the investigated specimens was measured using Vickers indenter and calculated according to ASTM: B933-09 while, compressive strength was measured according to ASTM E9. In addition, the values of elastic moduli; Young's modulus (L), shear modulus (G), elastic modulus (E), bulk modulus (B) and Poisson's ratio ( $\nu$ ) have been calculated according to Refs. [26,27].

### **2.5. Characterization of the sintered samples**

The formed phases in nanocomposite samples result from sintering process, were examined using X-ray diffraction (XRD) technique, "Philips PW 1373" X-ray powder diffractometer with CuK-Ni filtered radiation. In order to confirm the molecular structure of the prepared nanocomposites, Fourier transform infrared (Vertex 80, Bruker, Germany) spectroscopy was employed. FTIR absorption spectra of the tested specimens were immediately collected by attenuated total reflection (ATR) unit, at room temperature, in the wavenumber range 4000–400  $\text{cm}^{-1}$ , 60 scans at resolution 4  $\text{cm}^{-1}$ . Scanning electron microscopy (SEM, type Quanta FEG250) with accelerating voltage of 30 kV and magnification 10 $\times$  up to 300,000 $\times$  was employed to examine the microstructure of these samples.

### **2.6. Biomedical characterization**

#### **2.6.1. In vitro bioactivity assessment of sintered nanocomposites**

In vitro bioactivity of the resultant nanocomposites was evaluated by soaking samples in the simulated body fluid (SBF) prepared according to the recipe described by Kokubo *et al.* [28,29] while maintaining the ratio of glass grains to solution volume = 0.01 g/ml [30]. Subsequently, the soaked samples were subjected to XRD and SEM to examine the HA layer formed on their surfaces. The ionic concentrations of the prepared SBF compared to the human blood plasma concentrations are listed in Table 3.

## 2.6.2. Evaluation of the antibacterial effect of prepared samples

The antibacterial behavior of the prepared nanocomposites was tested against *S. aureus* (ATCC6538) and *E. coli* (ATCC25922) bacterial strains using disc-diffusion method at 37 °C for 24 h.

# 3. Results And Discussion

## 3.1. Physical and mechanical properties

It cannot be denied that the removal of porosity present in the sintered sample is the key factor in improving the densification behavior [31]. Moreover, the presence of nano-sized CHA powders helps to efficiently close the pores which consequently, leading to better densification behavior [32]. Also, the glass contents in the nanocomposites along with the chosen sintering temperature are expected to play an increasingly important role in enhancing the densification manner [33, 34]. As previously discussed in Refs. [17, 20], a good densification depends on the sintering temperature chosen as the sintering process is carried out through three stages. First, the compaction of powders facilitates contact formation. Second, the particles are closely bonded due to the creation of “necks” between them. Notably, these necks are formed when the sintering temperature reaches two-thirds of the melting point. Finally, the particles are fully bonded, and cannot be seen individually and the remaining porosity is closed-off. Based on these facts, bulk density and apparent porosity of the sintered nanocomposites were measured as shown in Fig. 1. It is evident from this figure that successive increases in BG content lead to noticed increases in bulk density. On the other hand, this increase in BG content is responsible for reducing the porosity of the sintered nanocomposites.

In general, better mechanical properties are observed for sintered glass compared to those of the original glasses given that they are highly dependent on sintering conditions [35]. Thus, microhardness, compressive strength, Young's modulus, elastic modulus, bulk modulus, shear modulus (G) and Poisson's ratio ( $\nu$ ) of all sintered nanocomposites were measured and represented in Figs. (2–4). All mechanical properties of the examined nanocomposites exhibit marked increases with successive increases in the BG content. It is observed that the previous mechanical values increase by 81, 85, 78, 72, 70, 78, 82%, respectively with ascending the BG content up to 20 wt.%. Therefore, additions of BG content with different values succeed in enhancing the mechanical properties. As will be discussed in the following section, despite the partial decomposition of CHA at this relatively low temperature forming a  $\beta$ -tricalcium phosphate ( $\beta$ -TCP;  $\text{Ca}_3(\text{PO}_4)_2$ ) and calcium borate (CB;  $\text{Ca}_3(\text{BO}_3)_2$ ) phases which in turn, leads to a noticed decrease in mechanical properties of sintered samples, this detrimental effect is compensated for by the presence of grain size in the nano-scale range which considerably improves the mechanical properties. The results obtained are in good agreement with those reported in Refs. [36–38]. It is worth to underline that understanding the relationships between porosity and mechanical properties is essential to take advantage of the porosity to optimize the bioactivity behavior of prepared samples without sacrificing their mechanical properties [18].

## 3.2. Characterization of the sintered samples

## 3.2.1. XRD analysis

It is well-established that heat treatment of prepared glass may lead to its conversion into corresponding glass-ceramic bearing in mind that the amount of residual glass composition and the resulting crystalline phases along with their quantities are highly dependent on the properties of the glass and the conditions of the heat treatment process [30]. Because of these facts, XRD technique should be used to determine the resulting phases as a result of heat treatment. Therefore, XRD patterns were recorded for all sintered nanocomposites specimens as shown in Fig. 5. A careful analysis of the obtained XRD patterns reveals the presence of characteristic peaks for CHA (JCPDS No. 19–0272) only for BG0 sample. However, the BG1 sample shows a slight decrease in the intensity of some of the peaks characteristic of CHA. This decrease may be attributed to the addition of 5 wt.% of BG, at the expense of CHA, or the very slight CHA degeneration and  $\beta$ -TCP formation that is below the XRD instrument detection limit. For the BG2 sample, these peaks appear alongside those of the  $\beta$ -TCP and the CB phases identified according to (JCPDS No. 03-0691) and (JCPDS No. 70–0868), respectively. By increasing the BG content in the investigated nanocomposites such as BG3 and BG4, the intensity of the peaks belonging to  $\beta$ -TCP and CB increase, while those belonging to CHA decrease. Meanwhile, the examined samples don't have a hump which indicates that the sintering temperature selected is sufficient to fully crystallize these glasses. These results ostensibly contradict those reported by Youness *et al.* [19] who found that CHA nanopowders prepared using a mechanochemical synthesis method possessed excellent thermal stability as they did not decompose even after exposure to 1000 °C. Following the explanation mentioned in Ref. [38], the presence of BG promotes the partial decomposition of CHA, at this lower sintering temperature, giving the characteristics peaks of the aforementioned phases due to the expulsion of some  $\text{OH}^-$  groups. However, the majority of the glass examined remains amorphous as indicated by the presence of its characteristic hump. The obtained results are in-line with those reported in Refs. [38, 39].

## 3.2.2. FTIR spectral analysis

In this study, FTIR infrared absorption measurements were employed to identify the main structural groups in the prepared samples. In this regard, FTIR absorption spectra were recorded for all as-prepared samples as shown in Fig. 6 taking into account that their assignment was carried out based on the literature [17, 40–44]. Although the prepared BG sample is mainly consisted of two formers, i.e.  $\text{B}_2\text{O}_3$  and  $\text{SiO}_2$ , the vibration modes recorded for the tested samples only belong to  $\text{B}_2\text{O}_3$ . On the other hand, those of  $\text{SiO}_2$  are absent. The reason for this result is that the added glass is rich in  $\text{B}_2\text{O}_3$  content while the  $\text{SiO}_2$  content is low (5%) and thus adding this glass system in successive proportions up to 20% is not sufficient to show the characteristic bands of  $\text{SiO}_2$ . Additionally, the characteristic band of the Ag-O vibration mode near  $565\text{ cm}^{-1}$  is absent due to the same cause described above for  $\text{SiO}_2$ . Since CHA has the major contribution to the studied nanocomposites, the characteristic bands for  $\text{PO}_4^{3-}$ ,  $\text{CO}_3^{2-}$  and  $\text{OH}^-$  groups appear. Of note, the partial decomposition of CHA and  $\beta$ -TCP phase formation can also be confirmed by FTIR spectroscopy. Careful analysis of the figure points out the following:

- Band near  $1630\text{ cm}^{-1}$  can be attributed to the vibrational mode of  $\text{OH}^-$  group. Compared to the FTIR spectrum of BG0, this band is less intense due to partial decomposition of CHA as a result of the presence of BG that promotes the degeneration of CHA molecules.
- Medium ill-defined band around  $1200\text{ cm}^{-1}$  may be attributed to the asymmetric stretching vibration of the B-O bond of the  $\text{BO}_4$  structural units considering that successive increases in the BG contents in the studied nanocomposites, at the expense of CHA, lead to an improvement in the appearance of this shoulder.
- Strong sharp band near  $1035\text{ cm}^{-1}$  with medium ill-defined one may be assigned to the symmetric vibrations of P-O of HA. It is worth to note that the maximum intensity is recorded for BG0 and BG1 samples having in mind that increases in BG content lead to a decrease in the band intensity. It is worth to note that the formation of  $\beta$ -TCP phase usually results in a noticeable shift of this band towards a higher wavenumber, i.e.  $1120\text{ cm}^{-1}$ . However, this effect is not observed as it is masked by bands belonging to  $\text{B}_2\text{O}_3$  and the un-degraded CHA besides the slight formation of such phase.
- Sharp strong band at  $940\text{ cm}^{-1}$  can be ascribed to the overlap of vibration modes of the B-O of  $\text{BO}_4$  units from diborate groups and O-P-O bond of the CHA. It should be noted that this band can also be assigned to the O-P-O bond of  $\beta$ -TCP phase. Notably, the decrease in CHA contents is responsible for the observed increases in the intensity of this band.
- Bands in the spectral region, i.e.  $500\text{--}800\text{ cm}^{-1}$  can be ascribed to the bending vibrations of different borate units.
- Two bands around  $560$  and  $603\text{ cm}^{-1}$  may be attributed to the bending vibrational mode of O-P-O in the  $\text{PO}_4^{3-}$  groups.
- Weak band located near  $470\text{ cm}^{-1}$  can be assigned to asymmetric stretching vibration of  $\text{PO}_4$ .
- The presence of  $\text{CO}_3^{2-}$  groups is confirmed by bands at  $875$ ,  $1435$  and  $1460\text{ cm}^{-1}$ . As expected, increasing BG contents are responsible for detected decrease in the characteristic bands of CHA.

### 3.2.3. Morphological characterization

It is well-established that suitable morphological features of materials determine, to a great extent, their clinical applications [16]. In this respect, SEM was carried out to examine the morphology of all samples as represented in Fig. 7 (a-e). It is possible to see from Fig. 7a the characteristic pattern of HA which is mainly composed of particles having a spherical shape with a number of needle shaped particles uniformly distributed into spherical particles. Figure 7b reveals the absence of these needles due to the addition of BG content. The reason for this observation is the good distribution of BG particles consistent with the partial decomposition of CHA that supports the results discussed in the XRD section. Most importantly, the nanocomposites' particles are still of small sizes and can be clearly seen individually with a relatively high number of porosity. This observation is strongly in agreement with the previously discussed density results. By increasing the BG content to 10 wt.%, as seen from Fig. 7c, the porosity considerably decreases along with enlargement of particles' sizes due to the formation of necks which

have a strong role in improving the densification behavior of the nanocomposites. Due to the formation of these necks, most particles are no longer seen individually. Figure 7d points out that increasing the BG content to 15 wt.% is responsible for better condensation behavior as indicated by increased particles' sizes and decreased porosity. As can be seen from Fig. 7e, most of the porosity disappears and not all of the particles can be seen individually. These demonstrated observations are well consistent with the results for XRD, density and porosity.

### **3.3. Biomedical characterization**

#### **3.3.1. In vitro bioactivity assessment of sintered nanocomposites**

##### **3.3.1.1. XRD analysis**

It is well known that dipping bioactive samples in SBF solution leads to fast precipitation of  $\text{Ca}^{2+}$  and  $\text{PO}_4^{3-}$  ions onto their surfaces. On this basis, all prepared samples were soaked in SBF solution for 10 days and then, underwent XRD technique to assess their bioactive behavior as shown in Fig. 8. Interestingly, all samples show good bioactivity but still the best one is the sample with the highest content of BG, i.e. BG4. It should be noted that regardless of the partial decomposition of CHA, this decrease is compensated for by the presence of BG which is well-known for better bioactivity compared to CHA. These results are in a good agreement with those reported by Refs. [45, 46]. Knowing the high solubility of  $\beta$ -TCP phase in the SBF solution from the literature [16, 27], it can be inferred that this phase is not present in the figure.

##### **3.3.1.2. Microstructural characterization by SEM**

Since the bioactive feature of a material is determined by its ability to create a HA-like layer on its surface after soaking in SBF solution, SEM was again used to inspect the surface of BG4 sample after being soaked in SBF solution for 10 days, at two different magnification powers, as shown in Fig. 9. Selection of the BG4 sample is based on the obtained XRD results which revealed that the best bioactivity was for the BG4 specimen. Depending on the increase in the BG content in the investigated specimen, the sample surface was covered with a dense HA layer whose morphology differs completely compared to the BG4 sample before soaking in SBF solution.

#### **3.3.2. Evaluation of the antibacterial effect of sintered nanocomposites**

Generally, implantation of biomaterials into the fractured human bones may lead to the acute/chronic infections due to the formation of biofilm [47]. Accordingly, the antibacterial effect of these samples was tested against *S. aureus* (ATCC6538) and *E. coli* (ATCC25922) as Gram + and Gram- bacteria, respectively using disc-diffusion method was determined as shown in Figs. 10 (a-e) and 11 (a-e). On the other hand, the diameter of inhibition zone around the investigated samples was measured and listed in

Table 4. Note that these strains were chosen for performing this test due to that they are considered as the most common reasons for serious complications for patients after surgery [48]. It can be seen that the increased BG contents are responsible for the antibacterial effect as the sample free of BG does not show an antibacterial effect. On the other hand, the BG4 sample shows the largest inhibition zone among all samples examined in the case of *S. aureus*. This observation is based on the fact that the antibacterial effect of the tested samples depends on the amount of Ag<sup>+</sup> ions released to inhibit bacterial growth. Obviously, the inhibition zone is not completely clear to the reader since the sample diameter is about 1 cm, and thus, most of inhibition zone recorded is covered by the shadow of the disc. Another reason for this unclearness is the low ratio of Ag along with the low added content of BG to CHA. Interestingly, there are several mechanisms to explain the antibacterial activity of Ag<sup>+</sup> ions taking into account that these mechanisms differ for different bacterial species. Firstly, Ag<sup>+</sup> ions disrupt the microorganism's metabolism and consequently, prevent its growth [49]. Second, it is able to impede bacterial cell wall. Third, it prohibits the synthesis of different types of proteins. Last, it inhibits bacterial nucleic acids synthesis. These results are highly supported by those discussed in the literature [50–53].

## 4. Conclusions

Nanocomposites have different contents of carbonated hydroxyapatite (CHA) and borosilicate bioactive glass (BBG), which have the composition: 5SiO<sub>2</sub>-45B<sub>2</sub>O<sub>3</sub>-20Na<sub>2</sub>O-25CaO-5Ag<sub>2</sub>O, were prepared using the mechanical alloying method. Then, the prepared nanocomposites were consolidated and sintered at 700 °C. The mechanical, physical, bioactivity and antibacterial properties were studied along with their characterization using various tools such as X-ray diffraction technique (XRD), Fourier transform infrared (FTIR) spectroscopy and scanning electron microscopy (SEM). The XRD results revealed that the selected sintering temperature caused complete crystallization to form calcium borate (CB) phase. However, the presence of BBG encouraged the partial decomposition of CHA giving a β-tricalcium phosphate (β-TCP) phase beside CHA. The results showed that all of the above properties improved due to successive increases in BBG contents. Based on these results, the prepared nanocomposites can be considered promising biomaterials for use in various biomedical applications.

## Declarations

## Acknowledgement

The authors would like to acknowledge university of Tabuk for the financial support under research Project Number S-1441-0023.

## References

1. V.A. Thampi, B. Subramanian, Bioactive glasses for orthopedic and orthodontic implant applications, *Elyns J. Mater. Sci. Tech.* 1 (1) (2017): 1-10.

2. N. Olivera, Y. Suc, X. Lua, P.-H. Kuo, J. Dua, D. Zhuc, Bioactive glass coatings on metallic implants for biomedical applications, *Bioact. Mater.* 4 (2019): 261-270.
3. Seyedmajidi, R. Rajabnia, M. Seyedmajidi, Evaluation of antibacterial properties of hydroxyapatite/bioactive glass and fluorapatite/bioactive glass nanocomposite foams as a cellular scaffold of bone tissue, *J. Lab. Physicians* 10 (3) (2018): 265-270.
4. A. Taha, R.A. Youness, M. Ibrahim, Biocompatibility, physico-chemical and mechanical properties of hydroxyapatite-based silicon dioxide nanocomposites for biomedical applications, *Ceram. Int.* 46 (2020): 23599-23610.
5. A. Taha, R.A. Youness, M.F. Zawrah, Phase composition, sinterability and bioactivity of amorphous nano-CaO-SiO<sub>2</sub>-CuO powder synthesized by sol-gel technique, *Ceram. Int.* 46 (2020): 24461-24471.
6. E.S. Thian, T. Konishi, Y. Kawanobe, P.N. Lim, C. Choong, B. Ho, M. Aizawa, Zinc substituted hydroxyapatite: a biomaterial with enhanced bioactivity and antibacterial properties, *J. Mater. Sci. Mater. Med.* 24 (2013): 437-445.
7. P. Bhattacharjee, H. Begam, A. Chanda, Development and physical, chemical and mechanical characterization of doped hydroxyapatite, *Int. J. Sci. Eng. Res.* 2 (4) (2011): 1-8.
8. H. Oonishi, Orthopaedic applications of hydroxyapatite, *Biomaterials* 12 (1991): 171-178.
9. L. Hench, R.J. Splinter, W.C. Allen, T.K. Greenlee, Bonding mechanisms at the interface of ceramic prosthetic materials  
*J. Biomed. Mater. Res.* 2 (1971): 117-41.
10. L. Hench, J.R. Jones, Bioactive glasses: frontiers and challenges, *Front Bioeng Biotechnol*, 3 (2015): 1-12.
11. Oonishi, L.L. Hench, J. Wilson, F. Sugihara, E. Tsuji, M. Matsuura, Quantitative comparison of bone growth behavior in granules of Bioglass (R), A-W glass-ceramic, and hydroxyapatite, *J. Biomed. Mater. Res.* 51 (1) (2000): 37-46.
12. Qi, H. Wang, Y. Zhang, L. Pang, W. Xiao, W. Jia, S. Zhao, D. Wang, W. Huang, Q. Wang, Mesoporous bioactive glass-coated 3D printed borosilicate bioactive glass scaffolds for improving repair of bone defects, *Int. J. Biol. Sci.* 14 (4) (2018): 471-484.
13. Pal, A. Sayana, A. Joshi, D. Juyal, *Staphylococcus aureus*: A predominant cause of surgical site infections in a rural healthcare setup of Uttarakhand, 8 (11) (2019): 3600-3606.
14. P. Valappil, D.M. Pickup, D.L. Carroll, C.K. Hope, J. Pratten, R.J. Newport, M.E. Smith, M. Wilson, J.C. Knowles, Effect of silver content on the structure and antibacterial activity of silver-doped phosphate-based glasses, *Antimicrob. Agents Ch.* 51 (12) (2007): 4453-4461.
15. Taherian, R. Rojaee, M. Fathi, M. Tamizifar, Effect of different sol gel synthesis processes on microstructural and morphological characteristics of hydroxyapatite-bioactive glass composite nanopowders, *J. Adv. Ceram.* 3 (3) (2014): 207-214.
16. A. Youness, M.A. Taha, M. Ibrahim, In vitro bioactivity, molecular structure and mechanical properties of zirconia-carbonated hydroxyapatite nanobiocomposites sintered at different temperatures, *Mater.*

- Chem. Phys. 239 (2020) 122011.
17. A. Youness, M.A. Taha, A.A. El-Kheshen, M. Ibrahim, Influence of the addition of carbonated hydroxyapatite and selenium dioxide on mechanical properties and in vitro bioactivity of borosilicate inert glass, *Ceram. Int.* 44 (2018): 20677-20685.
  18. A. Youness, M.A. Taha, H. Elhaes, M. Ibrahim, Molecular modeling, FTIR spectral characterization and mechanical properties of carbonated hydroxyapatite prepared by mechanochemical synthesis, *Mater. Chem. Phys.* 190 (2017): 209–218.
  19. A. Youness, M.A. Taha, H. Elhaes, M. Ibrahim, Preparation, FTIR characterization and mechanical properties of hydroxyapatite nanopowders, *J. Comput. Theor. Nanosci.* 14 (2017): 2409–2415.
  20. A. Youness, M.A. Taha, M. Ibrahim, Effect of sintering temperatures on the in vitro bioactivity, molecular structure and mechanical properties of titanium/carbonated hydroxyapatite, *J. Mol. Struct.* 1150 (2017) 188–195.
  21. B. Moustafa, M.A. Taha, Evaluation of the microstructure, thermal and mechanical properties of Cu/SiC nanocomposites fabricated by mechanical alloying, *Int. J. Miner. Metall. Mater.* (2020) In Press.
  22. B. Moustafa, W.S. AbuShanab, E. Ghandourah, M.A. Taha, Microstructural, mechanical and thermal properties evaluation of AA6061/Al<sub>2</sub>O<sub>3</sub>-BN hybrid and mono nanocomposite surface, *JMRT* 9 (6) (2020): 15486-15495
  23. S. AbuShanab, E.B. Moustafa, E. Ghandourah, M.A. Taha, Effect of graphene nanoparticles on the physical and mechanical properties of the Al2024-graphene nanocomposites fabricated by powder metallurgy, *Results Phys.* 19 (2020) 103343.
  24. A. Youness, M.A. Taha, A. El-Kheshen, N. El-Faramawy, M. Ibrahim, In vitro bioactivity evaluation, antimicrobial behavior and mechanical properties of cerium-containing phosphate glasses, *Mater. Res. Express* 6 (2019) 075212.
  25. A. Youness, M.A. Taha, M. Ibrahim, A. El-Kheshen, FTIR spectral characterization, mechanical properties and antimicrobial properties of La-doped phosphate based bioactive glasses, *Silicon* 10 (2018): 1151–1159.
  26. A. Youness, M.A. Taha, M. Ibrahim, In vitro bioactivity, physical and mechanical properties of carbonated-fluoroapatite during mechanochemical synthesis, *Ceram. Int.* 44 (2018): 21323-21329.
  27. A. Youness, M.A. Taha, M. Ibrahim, Dense alumina-based carbonated fluorapatite nanobiocomposites for dental applications, *Mater. Chem. Phys.* 25 (2021) 123264.
  28. Kokubo, H. Takadama, How useful is SBF in predicting in vivo bone bioactivity, *Biomater* 27 (15) (2006): 2907–2915.
  29. Kokubo, H. Kushitani, S. Sakka, T. Kitsugi, T. Yamamuro, Solutions able to reproduce in vivo surface-structure changes in bioactive glass-ceramics A-W, *J. Biomed. Mater. Res. A* 24 (1990): 721–734.
  30. M.A. Khalil, R.A. Youness, M.S. Amer, M.A. Taha, Mechanical properties, in vitro and in vivo bioactivity assessment of Na<sub>2</sub>O-CaO-B<sub>2</sub>O<sub>3</sub>-SiO<sub>2</sub> glass-ceramics, *Ceram. Int.* 44 (2018): 7867–7876.

31. Laasri, M. Taha, E.K. Hlil, A. Laghzizil, A. Hajjaji, Manufacturing and mechanical properties of calcium phosphate biomaterials, *C.R. Mecanique* 340 (2012): 715–720.
32. Bandyopadhyay, E.A. Withey, J. Moore, S. Bose, Influence of ZnO doping in calcium phosphate ceramics, *Mater. Sci. Eng. C* 27 (2007): 14–17.
33. A. El-Kheshen, M.F. Zawrah, M. Awad, Densification, phase composition, and properties of borosilicate glass composites containing nano-alumina and titania, *J. Mater. Sci. Mater. Electron.* 20 (2009): 637–643.
34. A. Abo-Mosallam, S.N. Salama, S.M. Salman, Formulation and characterization of glass-ceramics based on  $\text{Na}_2\text{Ca}_2\text{Si}_3\text{O}_9$   $\text{Ca}_5(\text{PO}_4)_3\text{F}$ - $\text{Mg}_2\text{SiO}_4$  system in relation to their biological activity, *J. Mater. Sci. Mater. Med.* 20 (12) (2009): 2385–2394.
35. Bellucci, A. Sola, A. Anesi, R. Salvatori, L. Chiarini, V. Cannillo, Bioactive glass/hydroxyapatite composites: mechanical properties and biological evaluation, *Mater. Sci. Eng. C* 51 (2015): 196–205.
36. Puttaswamaiah, M. Shafiulla, M. Haneef, M.R. Hallur, Mechanical characterization and SEM analysis of calcium silicate reinforced polyester laminate, *Int. J. Sci. Eng. Res.* 5 (6) (2014): 470–476.
37. Mehdikhani, G.H. Borhani, Crystallization behavior and microstructure of bioglass-ceramic system, *Int. Lett. Chem. Phys. Astron.* 14 (2013): 58–68.
38. Ravarian, F. Moztaizadeh, M.S. Hashjin, S.M. Rabiee, P. Khoshakhlagh, M. Tahriri, Synthesis, characterization and bioactivity investigation of bioglass/hydroxyapatite, *Ceram. Int.* 36 (2010): 291–297.
39. Ghomi, M.H. Fathi, H. Edris, Effect of the composition of hydroxyapatite/bioactive glass nanocomposite foams on their bioactivity and mechanical properties, *Mater. Res. Bull.* 47 (2012): 3523–3532.
40. Koohkan, T. Hooshmand, M. Tahriri, D. Mohebbi-Kalhari, Synthesis, characterization and in vitro bioactivity of mesoporous copper silicate bioactive glasses, *Ceram. Int.* 44 (2018): 2390-2399.
41. L. Siqueira, N. Maurmann, D. Burguêz, D.P. Pereira, A.N.S. Rastelli, O. Peitl, P. Pranke, E.D. Zanotto, Bioactive gel-glasses with distinctly different compositions: Bioactivity, viability of stem cells and antibiofilm effect against *Streptococcus mutans*, *Mater. Sci. Eng. C* 76 (2017): 233-241.
42. Wang, Y. Zhang, C. Lin, W. Zhong, Sol-gel derived terbium containing mesoporous bioactive glasses nanospheres: in vitro hydroxyapatite formation and drug delivery, *Colloids Surf. B: Biointerfaces* 160 (2017): 406-415.
43. Radev, I. Michailova, D. Zaimova, T. Dimova, In vitro bioactivity of Silver containing sol-gel glasses: FTIR analysis, *IJIR* 3 (4) (2017): 316-323.
44. Htut, M. Lwin, P. Kaung, S. Htoon, Infrared spectroscopic study on the structure of  $\text{Ag}_2\text{O} \cdot \text{B}_2\text{O}_3$  glasses, *Jour. Myan. Acad. Arts& Sc.* IV (2) (200): 339-346.
45. Manafi, F. Mirjalili, R. Reshadi, Synthesis and evaluation of the bioactivity of fluoroapatite-45S5 bioactive glass nanocomposite, *Prog. Biomater.* 8 (2019): 77-89.

46. Seyedmajidi, S. Seyedmajidi, H. Alaghehmand, K. Hajian-Tilaki, S. Haghanifar, E. Zabihi, R. Rajabnia, M. Seyedmajidi, Synthesis and characterization of hydroxyapatite/bioactive glass nanocomposite foam and fluorapatite/bioactive glass nanocomposite foam by gel casting method as cell scaffold for bone tissue, *Eurasian J. Anal. Chem.* 13 (3) (2018): 1-13.
47. Cabal, L. Alou, R. Couceiro, F. Cafini, R. Couceiro, L.E. Tejada, F. Guitian, R. Torrecillas, J.S. Maya, A new biocompatible and antibacterial free glass-ceramic for medical applications, *Sci. Rep.* 5440 (4) (2014): 1–9.
48. S. AbuShanab, E.B. Moustafa, M.A. Taha, R.A. Youness, Synthesis and structural properties characterization of titania/zirconia/calcium silicate nanocomposites for biomedical applications, *Appl. Phys. A* 126 (2020): 1-12.
49. N. Kim, Q.L. Feng, J.O. Kim, J. Wu, H. Wang, G.C. Chen, F.Z. Cui, Antimicrobial effects of metal ions ( $\text{Ag}^+$ ,  $\text{Cu}^{2+}$ ,  $\text{Zn}^{2+}$ ) in hydroxyapatite, *J. Mater. Sci. Mater. Med.* 9 (1998): 129-134.
50. L. Feng, J. Wu, G.Q. Chen, F.Z. Cui, T.N. Kim, J.O. Kim, A mechanistic study of the antibacterial effect of silver ions on *Escherichia coli* and *Staphylococcus aureus*, *J. Biomed. Mater. Res.* 52 (2000): 662–668.
51. Ranga, E. Poonia, S. Jakhar, A.K. Sharma, A. Kumar, S. Devi, S. Duhan, Enhanced antimicrobial properties of bioactive glass using strontium and silver oxide nanocomposites, *J. Asian Ceram. Soc.* 7 (2019): 75-81.
52. Ahmed, D. Ready, M. Wilson, J.C. Knowles, Antimicrobial effect of silver-doped phosphate-based glasses, *J. Biomed. Mater.* 79 (3) (2006): 618-626.
53. L. Percival, P.G. Bowler, D. Russell, Bacterial resistance to silver in wound care, *J. Hosp. Infect.* 60 (2005): 1-7.

## Tables

**Table 1: Nominal composition (wt.%) of  $\text{Ag}_2\text{O}$ -containing borosilicate glass.**

Content (wt.%)	Oxide
5	$\text{SiO}_2$
45	$\text{B}_2\text{O}_3$
20	$\text{NaO}$
25	$\text{CaO}$
4	$\text{Ag}_2\text{O}$

**Table 2.** Scheme of the prepared nanocomposites indicating the sample code and its composition as weight percentage (wt.%).

Hydroxyapatite (CHA)	Bioactive glass (BG)	Specimen code
100	0	BG0
95	5	BG1
90	10	BG2
85	15	BG3
80	20	BG4

**Table 3.** The ionic concentrations of the prepared SBF compared to those of human blood plasma.

Ion concentration (mM)								Solution
SO <sub>4</sub> <sup>2-</sup>	HPO <sub>4</sub> <sup>2-</sup>	HCO <sub>3</sub> <sup>-</sup>	Cl <sup>-</sup>	Ca <sup>2+</sup>	Mg <sup>2+</sup>	K <sup>+</sup>	Na <sup>+</sup>	
0.5	1.0	4.2	147.8	2.5	1.5	5.0	142.0	<b>SBF</b>
0.5	1.0	27.0	103.0	2.5	1.5	5.0	142.0	<b>Blood plasma</b>

**Table 4.** The measured inhibition zone diameters of all sintered nanocomposites against *S. aureus* and *E. coli* were shown.

Inhibition zone diameter (mm))		Sample code
<b>E. coli</b>	<b>S. aureus</b>	
Nil	Nil	BG0
Nil	Nil	BG1
Nil	11	BG2
11	11	BG3
11	12	BG4

## Figures

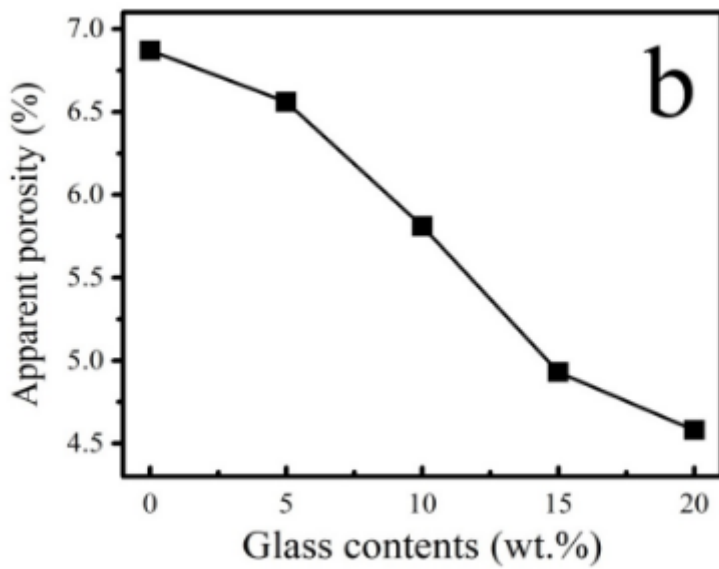
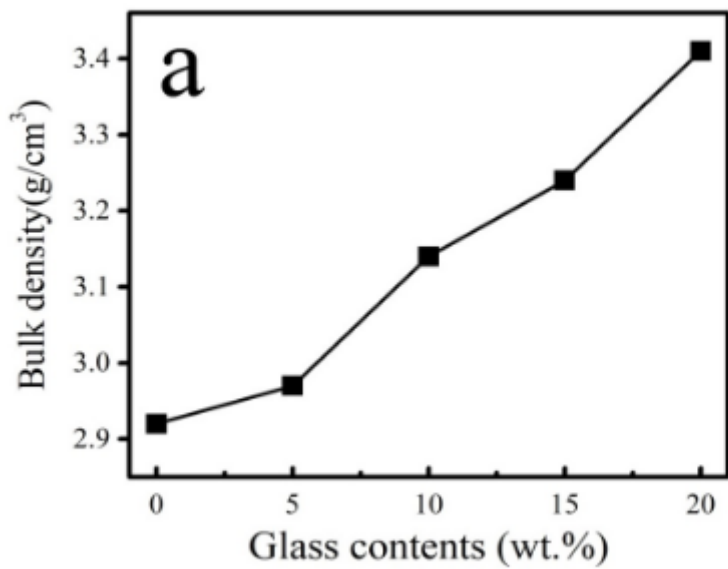


**Figure 1**

Based on these facts, bulk density and apparent porosity the sintered nanocomposites were measured as shown in Fig. 1.

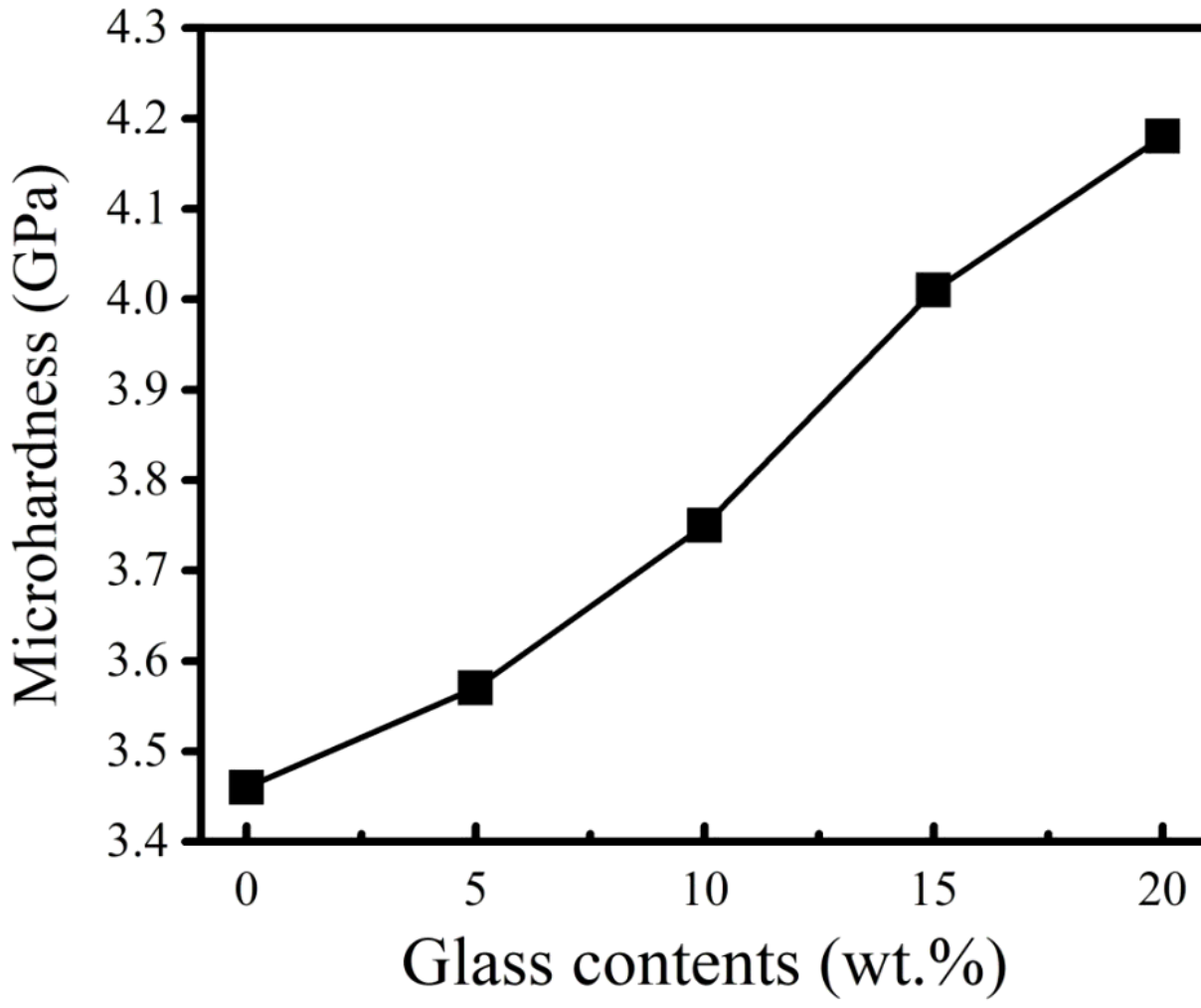
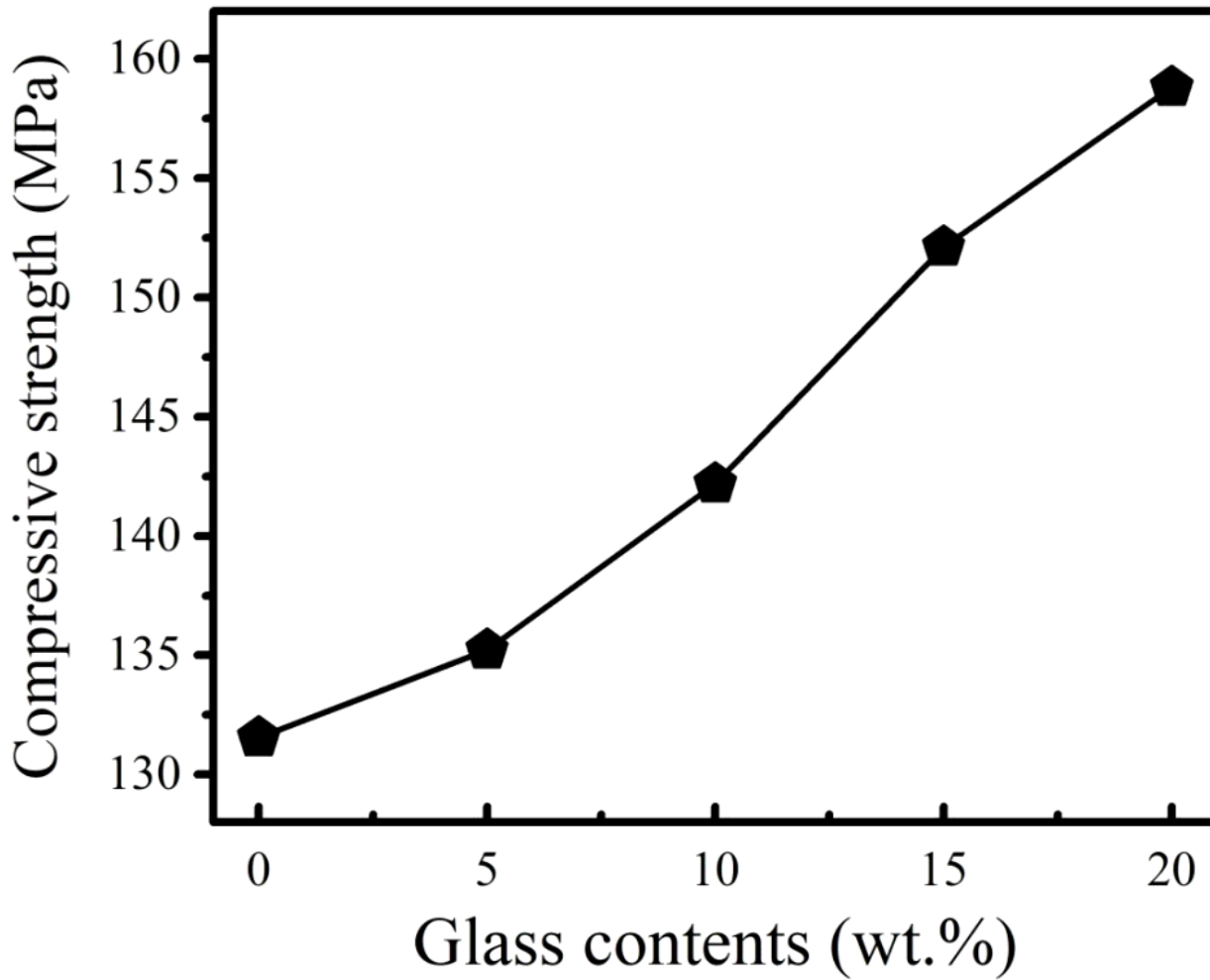


Figure 2

Young's modulus, elastic modulus, bulk modulus, shear modulus (G) and Poisson's ratio ( $\nu$ ) of all sintered nanocomposites were measured and represented in Figs. (2-4).



**Figure 3**

Young's modulus, elastic modulus, bulk modulus, shear modulus (G) and Poisson's ratio ( $\nu$ ) of all sintered nanocomposites were measured and represented in Figs. (2-4).

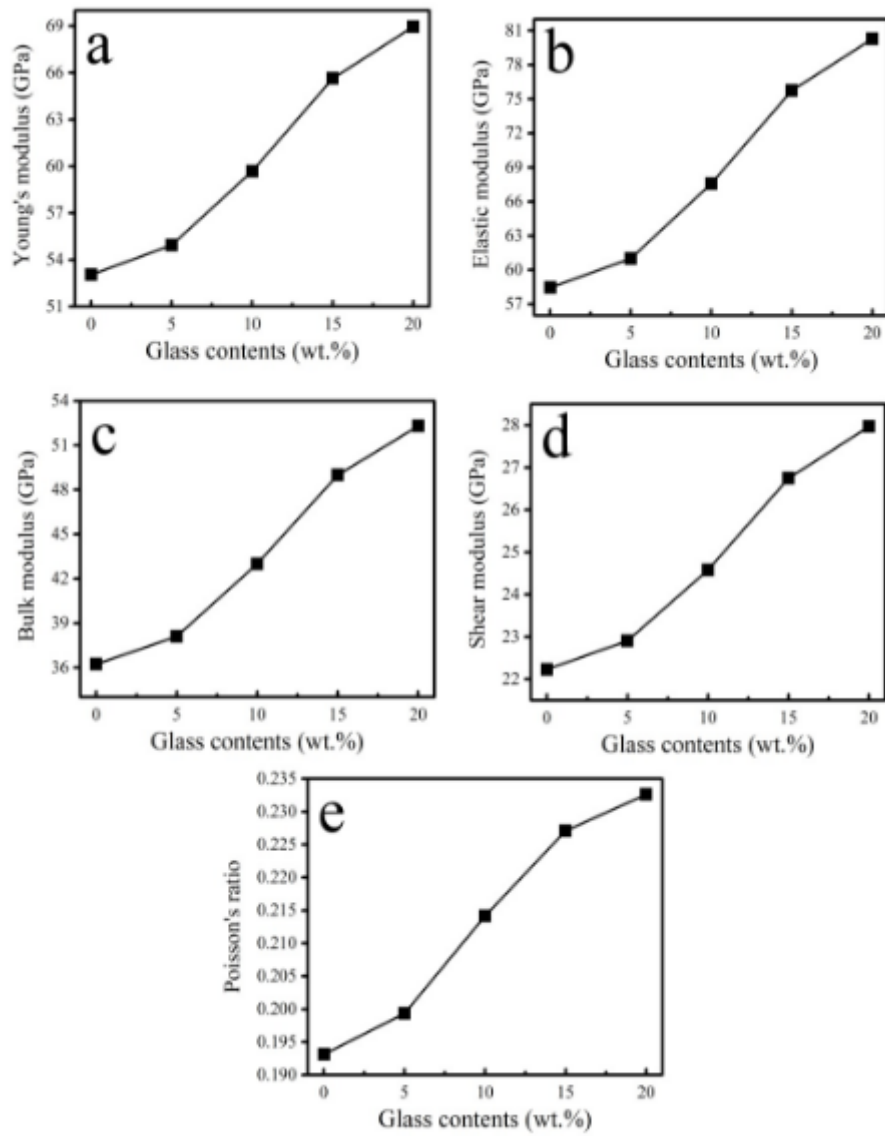


**Figure 4**

Young's modulus, elastic modulus, bulk modulus, shear modulus (G) and Poisson's ratio ( $\nu$ ) of all sintered nanocomposites were measured and represented in Figs. (2-4).

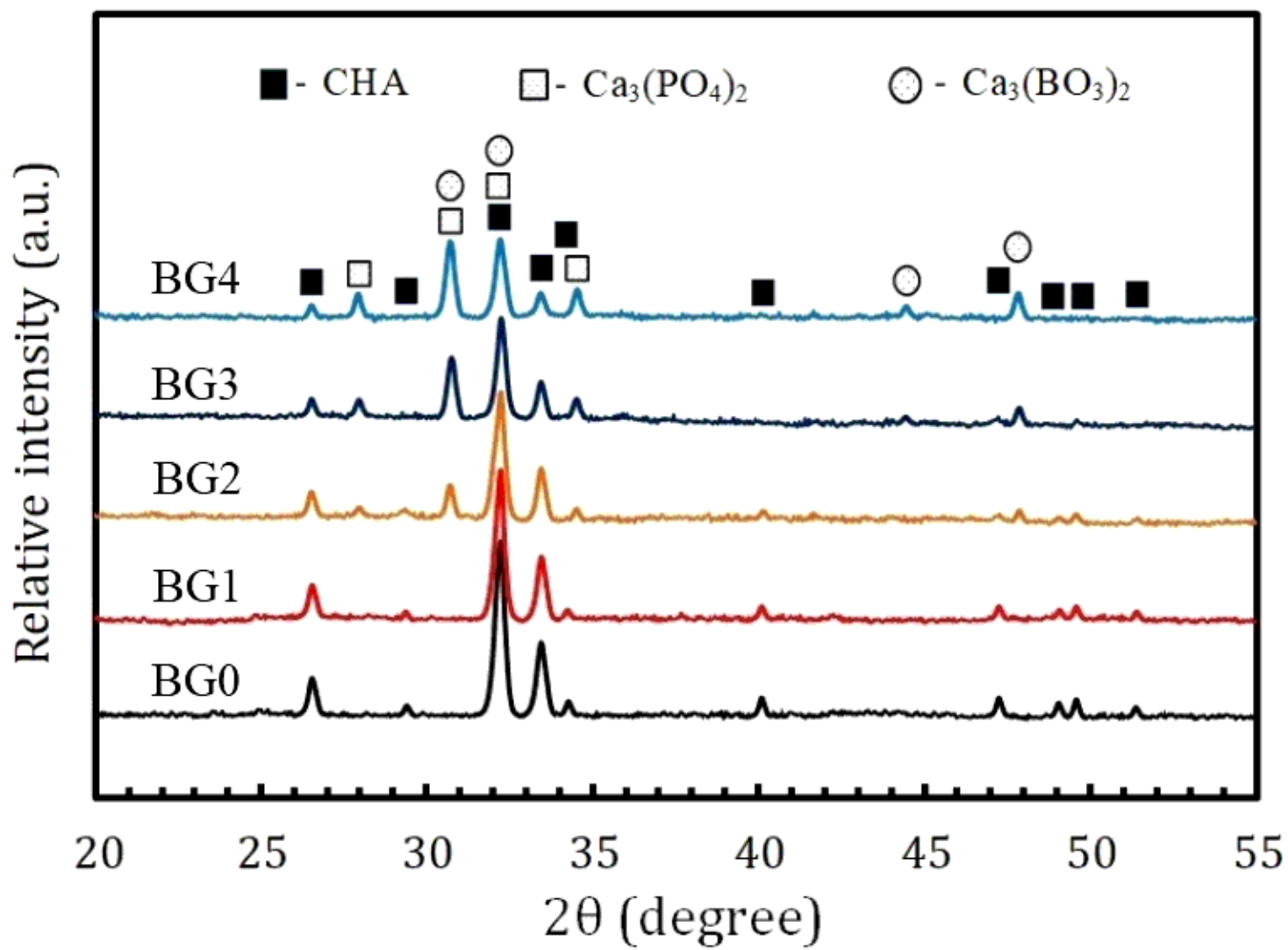


Figure 5

XRD patterns were recorded for all sintered nanocomposites specimens as shown in Fig. 5.

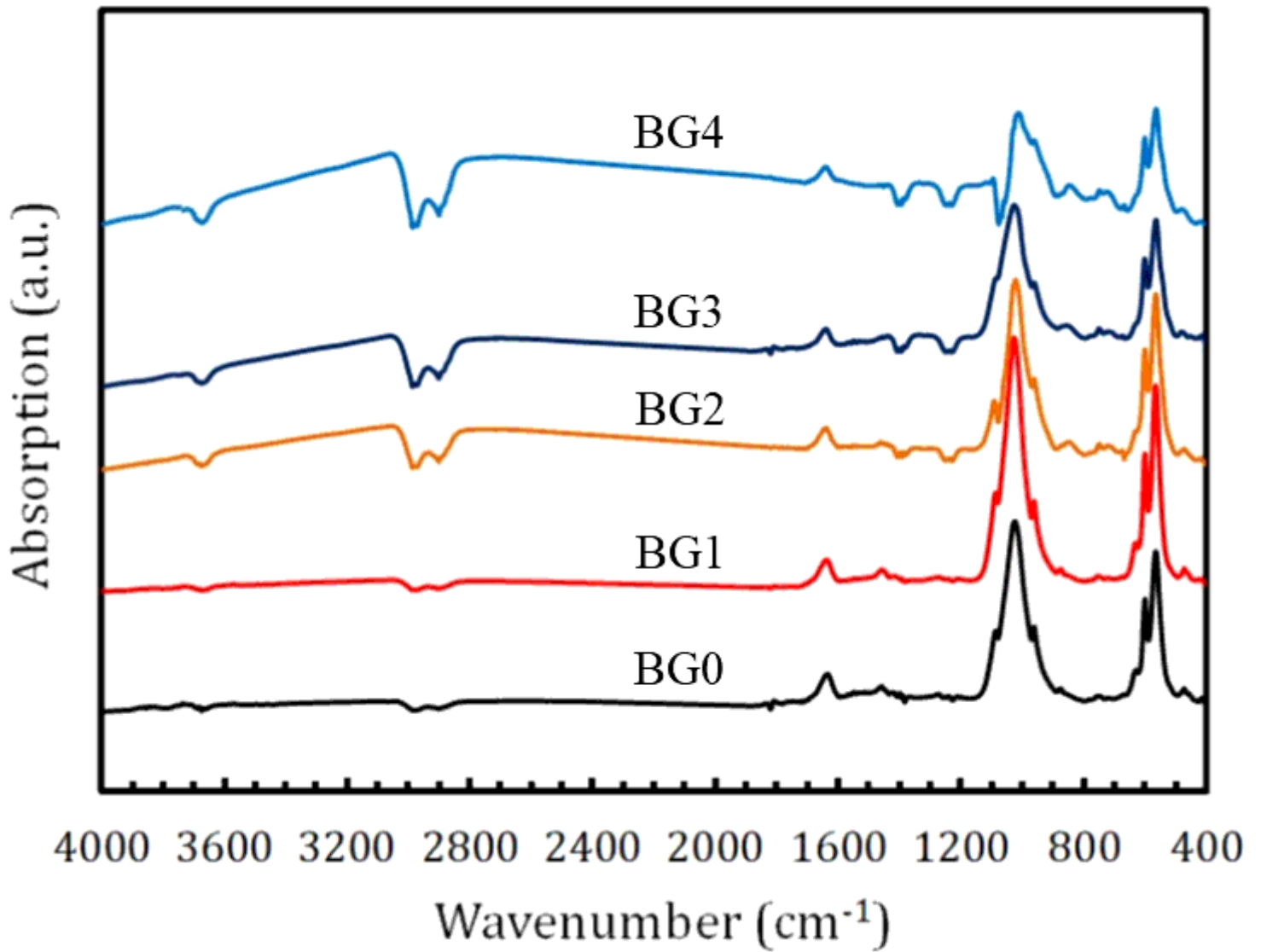
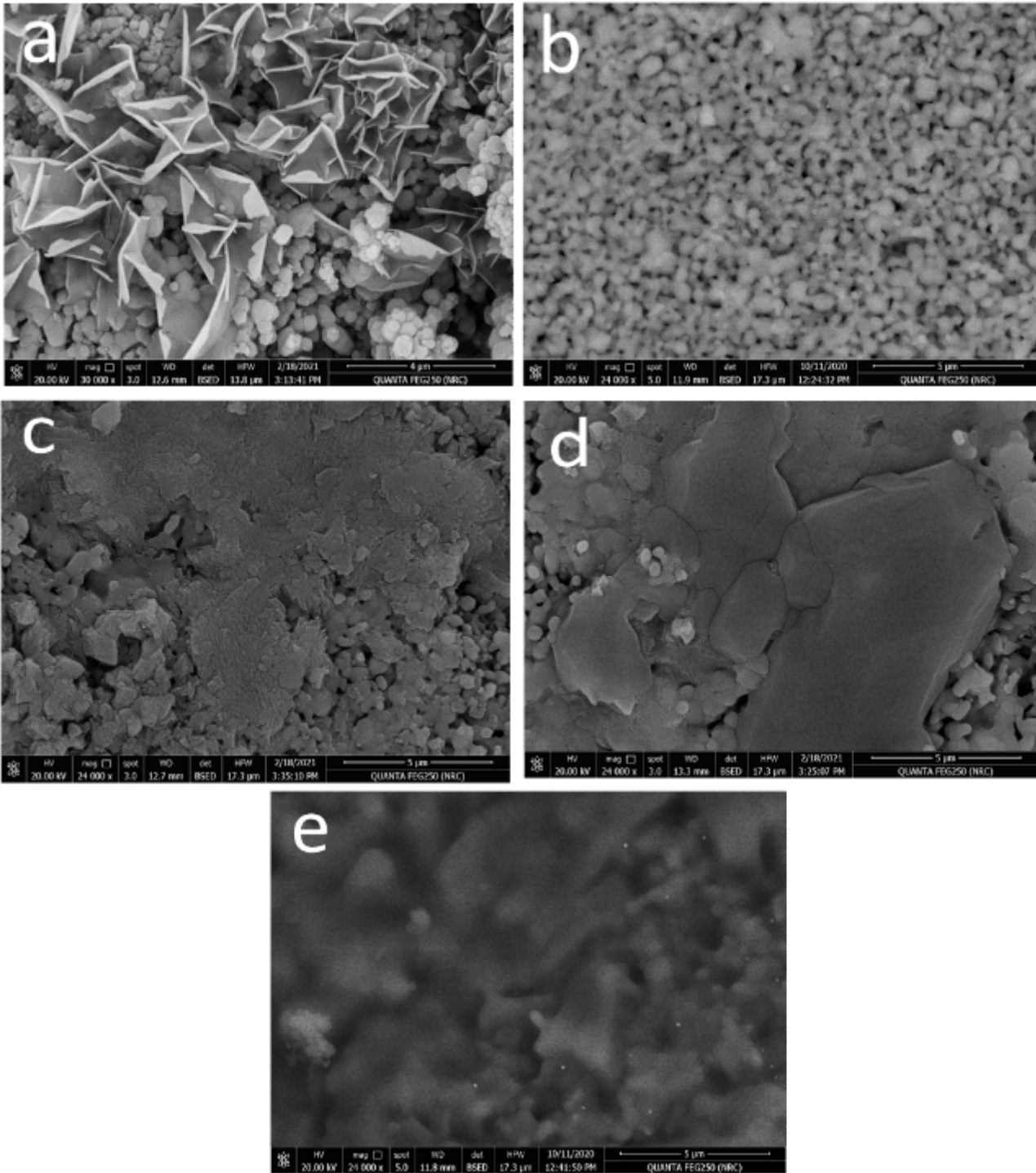


Figure 6

FTIR absorption spectra were recorded for all as-prepared samples as shown in Fig. 6 taking into account that their assignment was carried out based on the literature [17, 40-44].



**Figure 7**

In this respect, SEM was carried out to examine the morphology of all samples as represented in Fig. 7 (a-e). It is possible to see from Fig. 7a the characteristic pattern of HA which is mainly composed of particles having a spherical shape with a number of needle shaped particles uniformly distributed into spherical particles. Fig. 7b reveals the absence of these needles due to the addition of BG content.

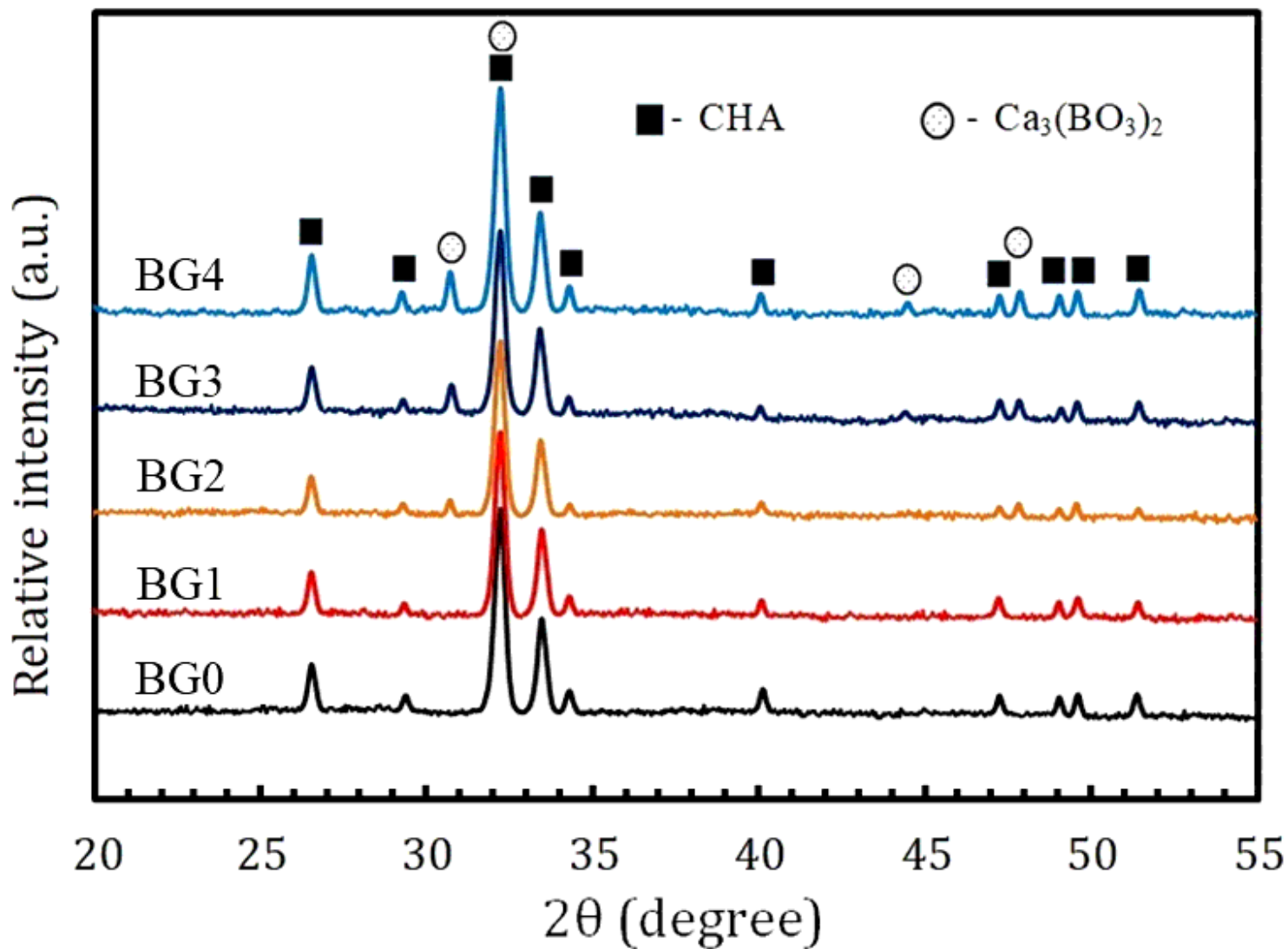
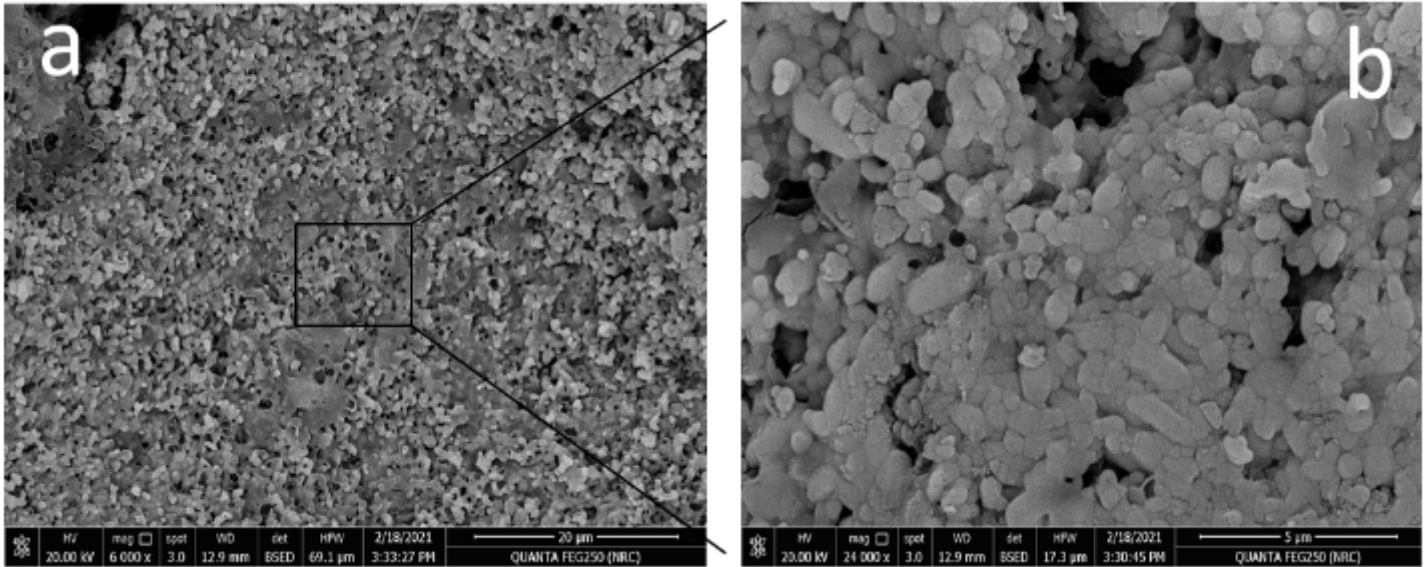


Figure 8

all prepared samples were soaked in SBF solution for 10 days and then, underwent XRD technique to assess their bioactive behavior as shown in Fig. 8.



**Figure 9**

SEM was again used to inspect the surface of BG4 sample after being soaked in SBF solution for 10 days, at two different magnification powers, as shown in Fig. 9.

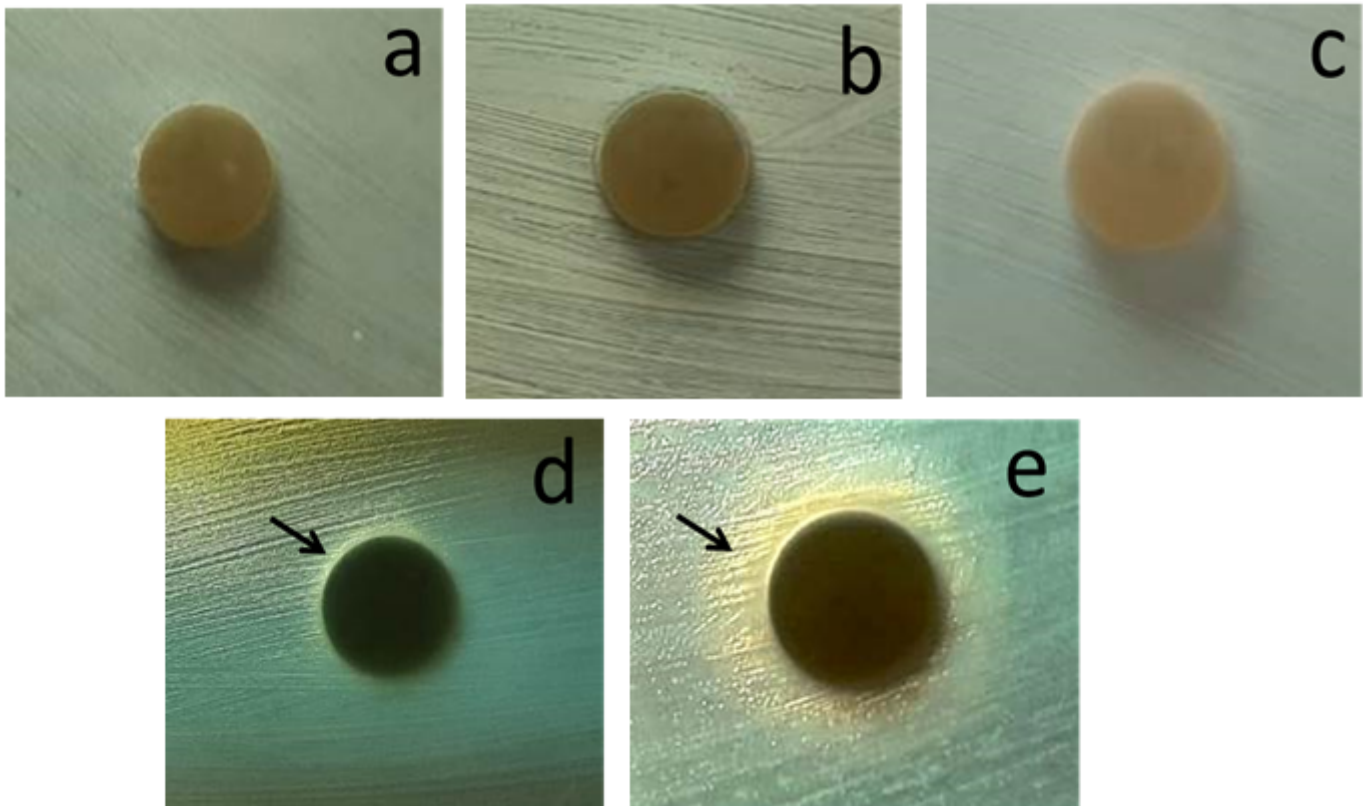


**Figure 10**

the antibacterial effect of these samples was tested against *S. aureus* (ATCC6538) and *E. coli* (ATCC25922) as Gram+ and Gram- bacteria, respectively using disc-diffusion method was determined as shown in Figs. 10 (a-e) and 11 (a-e).

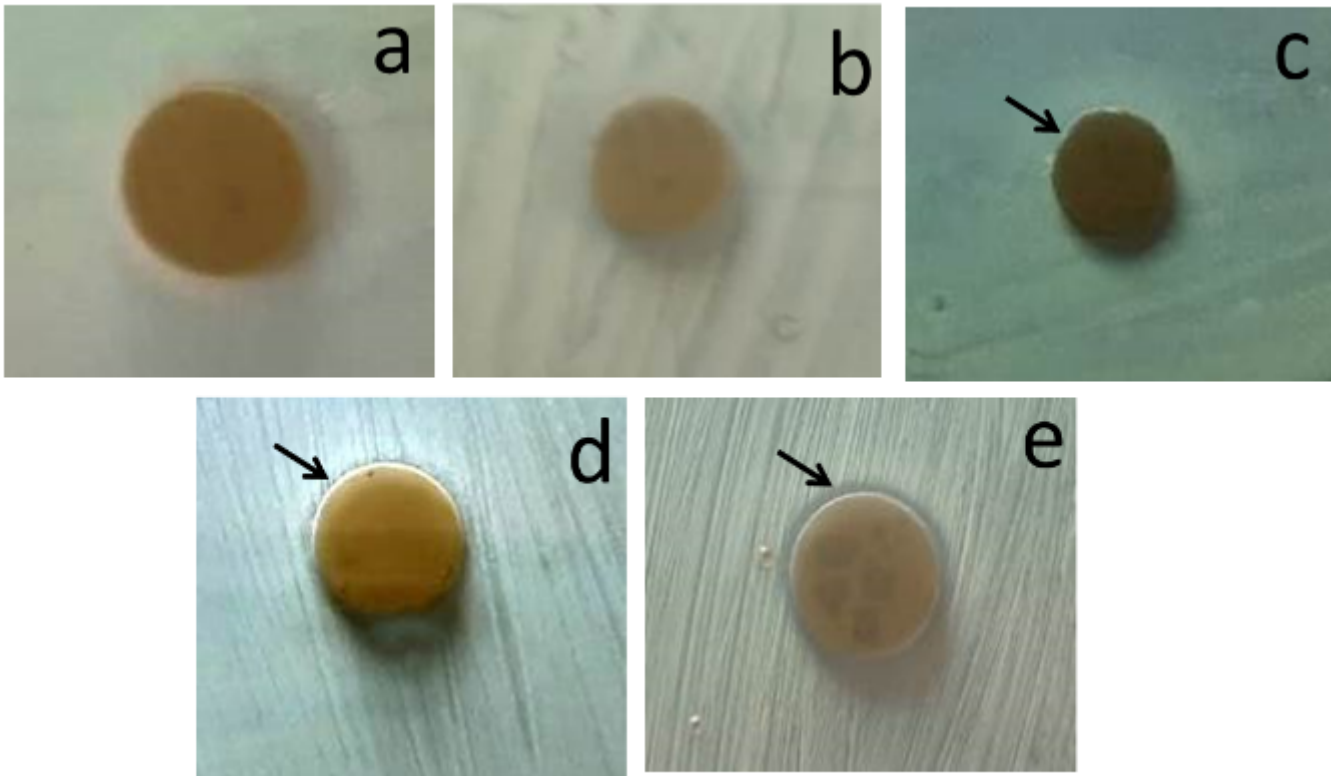


**Figure 11**

the antibacterial effect of these samples was tested against *S. aureus* (ATCC6538) and *E. coli* (ATCC25922) as Gram+ and Gram- bacteria, respectively using disc-diffusion method was determined as shown in Figs. 10 (a-e) and 11 (a-e).